



High-efficiency, single-crystalline, p- and n-type Si solar cells: Microstructure and chemical analysis of the glass layer

Praveen Kumar^{a,*}, Zainul Aabdin^b, Michael Pfeffer^a, Oliver Eibl^a

^a Institute of Applied Physics, Eberhard Karls University Tuebingen, Auf der Morgenstelle 10, 72076 Tuebingen, Germany

^b Institute of Materials Research and Engineering (IMRE), A*STAR, 2 Fusionopolis Way, Innovis, #08-03, Singapore 138634, Singapore

ARTICLE INFO

Keywords:

Crystalline Si solar cells
Glass phase
Chemical analysis
Specific contact resistance
Structure-property relationship

ABSTRACT

Recent investigations of the front side metallization of high-efficiency mono-crystalline Si solar cells proved that the glass layer formed at the Si/metallization interface during the screen printing plays an essential role for the charge transport, both in n- and p-type cells. High-efficiency cells (~ 18.0% for p-type and ~ 20% for n-type cells) show similar microstructure of the glass layer and similar temperature dependence of the series resistance. From this it is concluded that the microstructure of the glass layer determines the series and contact resistance of the front side metallization.

The glass layers of high-efficiency cells contain a high density of nano-Ag colloids and other precipitates which reduce the contact resistance. A percolation model was proposed and is best suited to describe the charge transport in a dirty semiconductor containing metallic precipitates.

Quantitative chemical composition of the glass layer of p- and n-type cells was investigated by Energy Dispersive X-ray (EDX) microanalysis in SEM and TEM. The chemical composition of the glass layer showed (SiO_x)Pb, as main constituents and Zn, Ti, Al, Ag, P and B as minor constituents with mole fractions above the detection limit of EDX. The glass layer is therefore considered to be a dirty semiconductor rather than a perfect insulator. The mole fractions of Zn (~ 1 at%) and Al (~ 1 at%) were quantitatively analyzed. Such analyses are important to correlate microstructural features with electrical properties of the front side metallization.

We could prove that in p-type cells the efficiency of the cells correlated with the chemical composition of the glass layer. In n-type cells, with Al-containing pastes EDX spectroscopy yielded Al beyond the detection limit in the glass layer, whereas for Al free pastes the Al mole fraction was below the detection limit of EDX and yielded reduced efficiencies. In p-type cells pastes with enhanced Zn mole fraction yielding zinc oxide phases in the bulk Ag finger and Zn mole fractions up to 5 at% in the glass layer.

1. Introduction

For standard screen printing technology, commercially available front side pastes (FSP) are mainly used for contacting phosphorous (P) and boron (B) doped emitters [1–15]. The FSP typically consist of silver (Ag) powders, glass frits, some organic binders and small amount of metallic additives and dopants such as zinc (Zn), aluminum (Al), titanium (Ti), B and P [1–3]. Due to the given chemical complexity, the exact composition of these pastes particularly the metallic additives and its effect on the contact quality is largely unknown.

The contact formation and phase forming reactions are given in Refs. [2,3,16]. Previous studies have shown that the front side Si/metallization interface consists of a Si emitter embedded with Ag nanocrystals [3–5], a glass layer typically < 1 μm thick that contains a high density of nano-Ag colloids and on top of it a bulk metallization finger

[6–11]. Depending on the chemical composition of the paste and firing conditions, microstructural features such as continuous or discontinuous wetting of the glass phase at the Si emitter and density of nano-Ag colloids can have a significant impact on the contact resistance and hence the efficiency of the cell [6–8].

In the literature, several models have been reported [3,4,10,17,18] considering the current path. Pyramidal Ag nanocrystals, 100 nm, in size, at the Si emitter were considered as essential together with tunneling through a thin glass layer. These models assumed that the glass layer was insulating and that tunneling might play a role. Table 1 summarizes an overview of the different models and their key statements published in the literature. In [6–8] we could prove that pyramidal Ag nanocrystals are not directly linked to a low contact resistance and that no evidence exists that the glass layer would be insulating. Tunneling in a rigid sense occurs over barriers usually only a

* Corresponding author.

E-mail address: praveen.kumar@uni-tuebingen.de (P. Kumar).

Table 1
Overview of the different models published in the literature.

Author	Citation	Proposed model
Schubert et al.	[3]	“Current transport via sparsely distributed direct interconnections between the Ag crystallites and the Ag bulk or via a tunneling through the modified glass layer between the Ag crystallites and the Ag bulk of the finger”
Ballif et al.	[4]	“Current flow from the emitter into the contact is not uniform, but occurs via a few isolated Ag crystallites that are directly connected to the Ag bulk of the contact, or, more likely, by tunneling through ultrathin glass layers”
Li et al.	[10]	“Microstructural observations suggest that a tunneling mechanism (likely assisted by nano-Ag colloids) is responsible for current extraction”
Kontermann et al.	[17]	“Silver crystals at the interface of silver thick film contacts play a major role for the current transport across such contacts, as only few crystals are in direct contact with the contact bulk”
Cabrera et al.	[18]	“Directly connected Ag crystallites at the pyramid tops play a major role in the solar cell's current conduction, while less current flows through the Ag crystallites separated from the silver finger by the glass and the nano-Ag colloids contained within the glass”

few nm thick. These thin barriers are not present in the glass layers and, therefore, these models do not describe the current path correctly.

The understanding of the formation of Ag crystallites in the literature is ambiguous, the effect of the glass chemistry and firing conditions on cell properties has not been carried out systematically. We found a systematic and convincing understanding for the formation of Ag nanocrystals based on our experimental findings and based on physical properties of the relevant material, i.e. Si. Si yields anisotropic surface properties, which strongly influence the electrical properties of interfaces [6]. This is now well known from Schottky barriers [19] for which it took decades to understand the physics correctly. A similar problem we have here with the screen printing metallization contacts [6].

There are four main microstructural findings summarized in our papers:

1. Formation of Ag nano-crystallites depends on the surface orientation of the Si [6,7].
2. $\langle 100 \rangle$ and $\langle 111 \rangle$ Si surfaces yield different shapes for the Ag nanocrystals: pyramidal for $\langle 100 \rangle$ and flat or pancake like for $\langle 111 \rangle$ [6,7].
3. n-type cells with B doped emitters do not show pyramidal Ag nanocrystals, independent of the paste chemistry and firing conditions, the reason for this has been explained in Ref. [8]. Such cells, however, yield a low contact resistance [8].
4. Textured $\langle 100 \rangle$ Si cells have predominantly $\langle 111 \rangle$ oriented surfaces and pyramidal Ag nanocrystals appear only at the edges of the Si pyramids [6,7].
Combining with electrical properties we concluded 3 additional findings:
5. Planar $\langle 100 \rangle$ Si cells yield pyramidal Ag nano crystallites and high contact resistances [6,7].
6. Planar $\langle 111 \rangle$ Si cells yield flat, pancake like Ag nanocrystals and low contact resistances [6,7].
7. In summary, pyramidal Ag nano crystals are not considered to be relevant for achieving low contact resistance. It is the shape of the nanocrystals that makes the difference, flat shaped is the more favorable shape, independent from paste chemistry and firing conditions.

Paste chemistry and firing conditions are important for the wetting behavior and, therefore, also for the series and contact resistance, it will however, not affect the properties of the Si metallization interface determined as outlined above. It means that e.g. paste chemistry and firing conditions cannot generate pyramidal crystals on $\langle 111 \rangle$ Si surfaces because this would contradict crystallographic arguments of the etching. Also independent of paste chemistry and firing conditions the strong anisotropy of the Si surface energy has to be taken into account: flat Ag nanocrystals will always appear on planar $\langle 111 \rangle$ Si surfaces, whereas pyramidal shaped Ag nanocrystals will appear on $\langle 100 \rangle$ Si surfaces. This is also based on a crystallographic argument: $\langle 111 \rangle$ are close packed planes in fcc structures. In summary, pastes that show favorable wetting behavior due to their chemistry and

firing condition generate a higher interface area that is electrically active and thus lower the contact resistance.

Recently, it has been reported that a more pronounced wetting of the glass layer and a high density of nano-Ag colloids in the glass layer serve as a quality criterion for achieving a low contact resistance [6–11]. The density of such nano-Ag colloids in the glass layer plays a key role for the charge transport through the glass layer [6,8,20]. Since the resistivity of the glass layer is assumed to be significantly lower with nano-Ag colloids present in the glass layer and based on that a percolative charge transport model has been introduced [6,8,20].

There are few experimental evidences that show that the glass layer itself contributes to the current conduction: forming gas annealing (FGA) treatment as reported by a number of groups had significantly improved both the contact resistance and conductivity of the glass layer [2,21–24]. Also rapid thermal annealing process introduces oxygen vacancies in the glass layer. Since the high-temperature firing process was applied for the screen printing and oxygen vacancies are formed at high temperatures [25] and will be partially preserved by a rapid thermal annealing at room temperature. Together with oxygen vacancies charge carriers are being generated and might yield a moderately semiconducting glass layer instead of an insulating.

The electrical resistivity of glasses with different compositions was investigated by Zhang et al. [26] with respect to the band gap of the glass and contact resistance values of about $1 \Omega \text{ cm}^2$ were achieved for such contacts. This shows the importance of monitoring the chemical composition of the glass layer for achieving lower contact resistances.

A number of papers were published underlying the effect of the glass frit chemistry, Ag particle size and influence of the firing conditions on the microstructural and electrical properties of the cells [1,2,10,21,22]. Although, the presence and significance of the glass layer was identified long time ago [1,3,4], the chemical analysis of the glass layer is hardly found in the literature, particularly important is the quantitative chemical analysis of the glass layer. It even appears that a certain composition is assigned to the glass layer [3,4,22], which we will prove not to be the case. The glass phase contained Si, Pb, and O as main constituents wherein Zn, Ti, Ag and other elements were dispersed in the glass layer [6–8].

In the present study, we take a correlative approach by applying both the SEM-EDX and analytical TEM-EDX spectroscopy in order to quantify the chemistry and microstructure of the glass layer on a sub- μm scale. By this approach, we obtained unprecedented insights about the role of the glass layer and established a cross-correlation to the electrical losses across the contact interface.

Dark-field images in combination with diffraction patterns were applied to investigate the structural features of the glass layer. We studied two p-type and one n-type cells processed with different front side metallization pastes. The quantitative chemical analysis of the glass layer on a sub- μm scale yields new possibilities for understanding and optimizing the chemical composition of the glass layer and hence the efficiency of the solar cell.

Table 2

Process parameters and electrical results of the large cell wafer ($15.6 \times 15.6 \text{ cm}^2$) such as firing temperature T_{FFO} and efficiency η are summarized in Table 1. These measurements were carried out by a commercial solar cell tester at Institute for Solar Energy (ISE) Fraunhofer for p-type cells and ISC-konstanz for n-type cells. Specific contact resistance ρ_c was measured on small sized solar cell by the TLM method.

Cell	Solar cell	Paste	T_{FFO} [°C]	η (%)	ρ_c [$\text{m}\Omega \text{ cm}^2$]
#1	p-type Si	FSP1	900	16.9	21
#2	p-type Si	FSP2	900	17.8	4.7
#3	n-type Si	AgAl	830	19.96	< 4

2. Experimental details

2.1. Solar cells processing and electrical characterization

In this study, p-type textured cells were processed on Cz grown $< 100 >$ Si wafers with P doped emitters. The emitter sheet resistance of $\sim 75 \Omega/\text{sq}$ was measured for p-type cells. [9]. Details of the solar cells processing of p-type cells are described in Refs. [6,7,9]. Large area ($15.6 \times 15.6 \text{ cm}^2$) n-type PERT (Passivated Emitter Rear Totally Diffused) cells with B doped emitters were fabricated on Cz grown $< 100 >$ Si grown wafers with base doping of $3 \Omega\text{-cm}$ and sheet resistance of $66 \Omega/\text{sq}$. [8]. For details see Refs. [8,27]. Cells #1 and #2 with P doped emitters (p-type) were contacted with two different front side metallization paste FSP1 and FSP2, respectively, while cell #3 with B doped emitter (n-type) was processed with an AgAl paste. All cells were optimally fired at their set peak temperatures (for details see Table 2).

The electrical properties and processing parameters of cells are listed in Table 2. Cells #1 and #2 contacted with front side paste FSP1 and FSP2, yielded maximum efficiencies of 16.9% and 17.8%, respectively, while cell #3 contacted with paste AgAl yielded the highest efficiency of about 20%. In addition, contact resistance measurements were carried out on small stripes typically $1 \times 1.5 \text{ cm}^2$ in size by the TLM (transmission line model) method. Cell #1 showed the highest contact resistance of $20 \text{ m}\Omega \text{ cm}^2$ whereas the contact resistance of cells #2 and 3 was smaller than $5 \text{ m}\Omega \text{ cm}^2$.

2.2. SEM and TEM specimen preparation and strategy for quantitative chemical analysis

Samples were prepared by conventional mechanical grinding followed by polishing and ion-milling steps and analyzed in both plan view and cross-section, for details see Refs. [6–9]. SEM EDX analyses was carried out at low primary energy to improve the lateral resolution of the method, typically a primary energy of 5 keV was selected. A detailed investigation of the microstructural and chemical analysis of the glass layer was carried out by TEM-EDX. The resolution in TEM is significantly better than in the SEM and best suited to precisely measure the glass layer. TEM-EDX spectroscopy is the method of choice for quantitative chemical analysis because of its high-lateral resolution and detection limit in the range of 1 at%.

Dark-field images in combination with diffraction patterns were applied to investigate the structural features of the glass layer. To investigate the different phases presented at the contact interface, we used superimposed energy-filtered TEM (EF-TEM) imaging techniques (referred to as RGB imaging) by making a colorful phase map of the area under investigation. RGB imaging was performed by acquiring three EF-TEM images at energy losses of 16 eV (Si plasmon peak), 24 eV (SiO_2 plasmon peak, Ag plasmon peak, Pb-O_{45} edge) and 32 eV (2nd Si plasmon peak), with an energy slit aperture of 5 eV width. Then, the three EF-TEM images were superimposed by assigning a false color to each of the EF-TEM image as 16 eV (Red), 24 eV (Green), and 32 eV (Blue) to yield a superimposed EF-TEM or RGB image. High-magnification bright and dark-field images of the glass layer were acquired

with an energy slit of 10 eV. Diffraction patterns were acquired with a selected area electron diffraction of about 750 nm in size.

The TEM is equipped with a LaB₆ filament, typical beam diameter of about 30 nm, an EDX detector and a low-background specimen holder for chemical analysis with an energy resolution of 136 eV at the Mn-K α line. All acquired spectra were quantitatively analyzed by applying the Cliff-Lorimer k factor method as described in Refs. [28–30]. EDX spectra were acquired with a spot size of 32 nm and an acquisition time of 300 s with a stray aperture to avoid stray radiation and to improve the detection limit. The counts of the Si peak were larger than 4000 for EDX spectra acquired in the glass layer.

3. Results

For high-efficiency cells ($\sim 18.0\%$ for p-type and $\sim 20\%$ for n-type cells) we observed similar microstructure of the glass layer (Fig. 1c, p-type, cell #T2 processed with paste FSP2 and Fig. 1d n-type, cell #T3 processed with paste AgAl), i.e. a matrix with a high density of Ag colloids covering the emitter and the Ag bulk. Besides the Ag colloids smaller precipitates were found in the glass layer. In addition, the temperature dependent series resistance (see Fig. 1a, p-type, cell #T2 processed with paste FSP2 and Fig. 1b, n-type, cell #T3 processed with paste AgAl) is similar for n- and p-type cells, both in absolute values and with respect to the temperature dependence. Series resistance measurements were carried out on small cells typically $1 \times 1 \text{ cm}^2$ under dark conditions. The series resistance was only weakly temperature dependent for both high-efficiency p- and n-type cells. We assume that the charge transport is limited by the glass layer which contains a high density of Ag colloids and other precipitates. In addition, p- and n-type cells showed a low series resistance, lower than $60 \text{ m}\Omega$. The reason for this low series resistance was explained in [8]: (i) dark measurements use carriers injected into the contacts and the current crossing the junction is in-homogenous and flows only underneath the contacts [8]. In case of illuminated measurements, the current crossing the junction is more uniform and flows along the emitter to the contacts. This current will be affected by the sheet resistance of the emitter. In summary, in the dark condition most of the current crosses the junction underneath the contact and therefore yields a low series resistance as compared to cells under illumination [8], for which a larger series resistance should be measured.

As a third point the chemical composition measured by EDX spectroscopy (Fig. 1e, p-type, cell #T2 processed with paste FSP2 and Fig. 1f, n-type, cell #T3 processed with paste AgAl) of the glass layer both for n- and p-type cells is similar. Therefore, it is concluded that the microstructure of the glass layer determines the series and contact resistance of the front side metallization. This is the main outcome of the detailed analyses we have carried out [6–8].

These investigations also proved the relevance of the glass layer for the current path for both n- and p-type cells. Low-efficiency cells showed significantly different microstructure and series resistance at the metallization interface.

In our previous work [20], n- and p-type cells processed with different front side pastes were investigated as shown in Fig. 2. A low Ag colloid density (see Fig. 1c, n-type cell processed with paste Ag, and Fig. 1d, p-type cell processed with paste FSP1) yielded a high contact resistance and a high colloid density (see Fig. 1a, n-type cell processed with paste AgAl and Fig. 1b, p-type cell processed with paste FSP2) was linked to a low contact resistance. This confirms that high-efficiency cells always yield the lowest contact resistances and a higher density of Ag colloids in the glass layer. Based on the above arguments and chemical analysis of the previous work (see Table 3) we assume that the glass layer is a dirty semiconductor. “Dirty semiconductor” means that the glass contains precipitates on a smaller length scale as compared to the Ag colloids and point defects such as impurities and oxygen vacancies yielding a semiconducting behavior. Moreover, screen printed front side pastes are subjected to a rapid thermal annealing process that

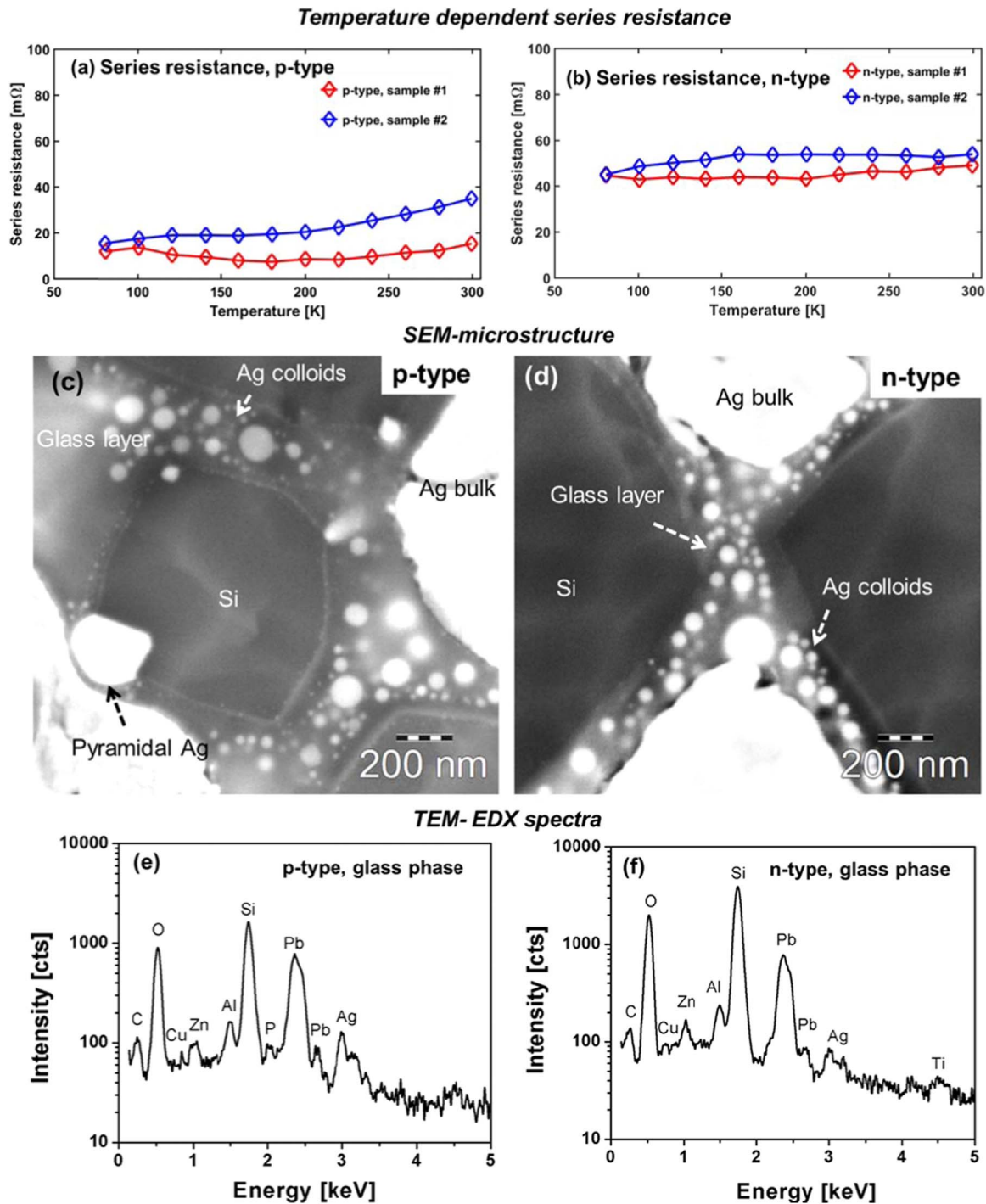


Fig. 1. Show the essential features of the high-efficiency p- and n-type cells: (a, c and e) for high-efficiency p-type cell processed with paste FSP2 and (b, d and f) for high-efficiency n-type with paste AgAl. (a–b) temperature dependent series resistance, (c–d) microstructure at the Si/metallization interface by SEM and (e–f) TEM-EDX spectra of the glass layer.

might introduce oxygen vacancies instead of ideal glass layer which yields a stoichiometric composition. Oxygen vacancies are known to generate n-type conductivity in oxides [25]. From this starting point a percolation model has been proposed [20], in which the microstructural features were introduced and the main features of the model are: (i) a finite electrical resistance of the glass layer and, (ii) colloids reducing the resistance of the individual current paths in a simple geometrical sense.

Different cells that were identically processed up to the front side metallization were screen printed with different pastes yielding significantly different contact resistances and efficiencies (Table 2). The

glass layer of such cells was investigated by EDX spectroscopy in the SEM and for a sub-group also by EDX spectroscopy in the TEM (Table 3). Usually, the paste specific features are not transmitted by the paste manufacturer, but can be identified in the glass layer (Table 4): (i) a Zn-rich paste yielded also a Zn-rich glass layer and (ii) an Al-free paste did not show Al in the EDX spectra of the glass layer. EDX spectroscopy is, therefore, very well suited to identify chemically specific properties of the glass layer, even when the paste features are not known or transmitted by the paste manufacturer. In summary the benefit of such analysis is twofold: (i) with respect to technology, i.e. the glass layer chemical composition depends on the properties of the paste and the

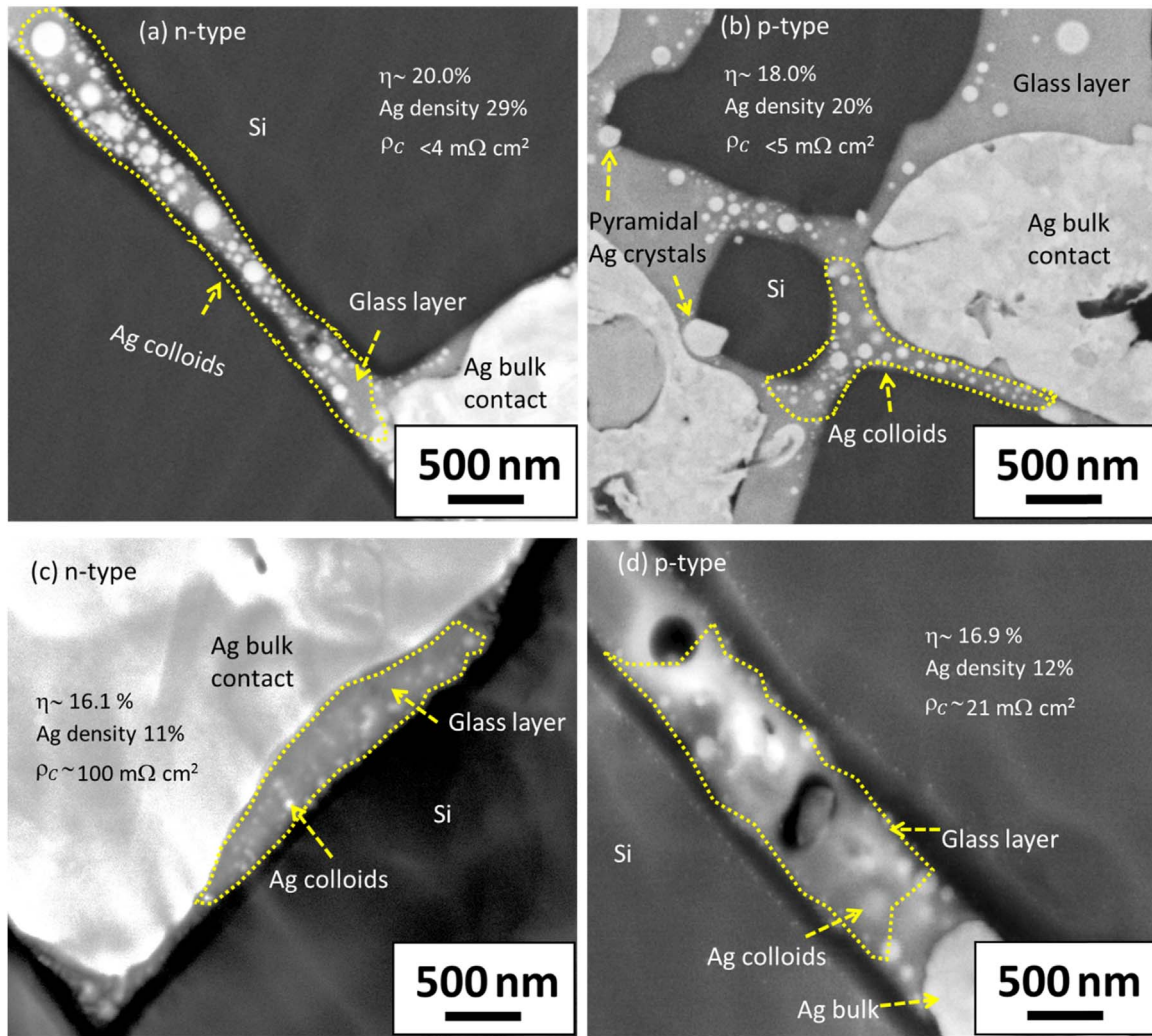


Fig. 2. Plan-view SEM images of the Si/metallization interface of n-type cells processed with paste AgAl (see a) and paste Ag (c) and p-type cells processed with paste FSP2 (see b) and paste FSP1 (d). The higher density of Ag colloids in the glass layer is clearly visible for the high-efficiency n- (a) and p- type cells (see b) [16].

Table 3

Overview of the chemical analysis of p- and n-type cells processed with different front side pastes and investigated by SEM-EDX and TEM-EDX spectroscopy as published in our previous work.

	Solar cell	Paste	SEM-EDX	TEM-EDX	Reference
1	p-type Si	FSP1	x	This work	[6,7]
2	p-type Si	FSP1	x	x	[6,7]
3	p-type Si	FSP2	x	This work	[6,7]
4	n-type Si	AgAl	x	This work	[8]
5	n-type Si	AgAl	x	–	[8]
6	n-type Si	Ag	x	–	[8]

Table 4

Summarizes the paste features such as Zn rich and containing Al in the glass layer as identified by SEM and TEM-EDX microanalysis.

	Solar cell	Paste	Paste features	SEM-EDX	TEM-EDX
	p-type, cell #1	FSP1	Zn rich	x	x
	n-type, cell #3	AgAl	contains Al	x	x

firing condition and (ii) with respect to the percolation model, metallic impurities affect the resistance of the glass layer. In addition, metallic precipitates will be formed in the glass layer that reduce the total contact resistance.

3.1. Microstructural analysis of the glass layer by TEM

A detailed description of the bright and dark-field images of the Si/metallization interface of cell #1 can be found in the [Supporting information S1](#). The important features of cell #1 are: (i) a small density of Ag colloids in the glass layer, (ii) small pockets of the SiN_x layer at the Si/metallization interface, and (iii) Zn rich oxide phases in the glass layer.

Fig. 3a is a low-magnification bright-field image of the Si/metallization contact interface of cell #2. Areas with and without SiN_x layer can be identified at the Si/metallization interface. The density of nano-Ag colloids (with sizes between 5 and 150 nm) is significantly increased in the glass layer of cell #2 (**Fig. 3a** right side) as compared to cell #1. **Fig. 3b** is the corresponding dark-field image of the same region. **Fig. 3c–d** are magnified parts of the glass layer. In **Fig. 3c** besides the nano-Ag colloids, small precipitates of sizes < 10 nm are present in the glass layer, however their nature remains unclear due to their small size.

Diffraction patterns and dark-field images were obtained on the glass layer of cell #2 and are shown in **Fig. 4a–d**. Diffraction patterns were acquired with a selected area aperture of about 750 nm in size. The diffraction patterns contain 3 features: (i) amorphous circular structures, (ii) ring patterns due to precipitates in the glass and, (iii) reflections of the monocrystalline Si. Note the large number of reflections on the ring structures in the pattern. The diffraction pattern can be

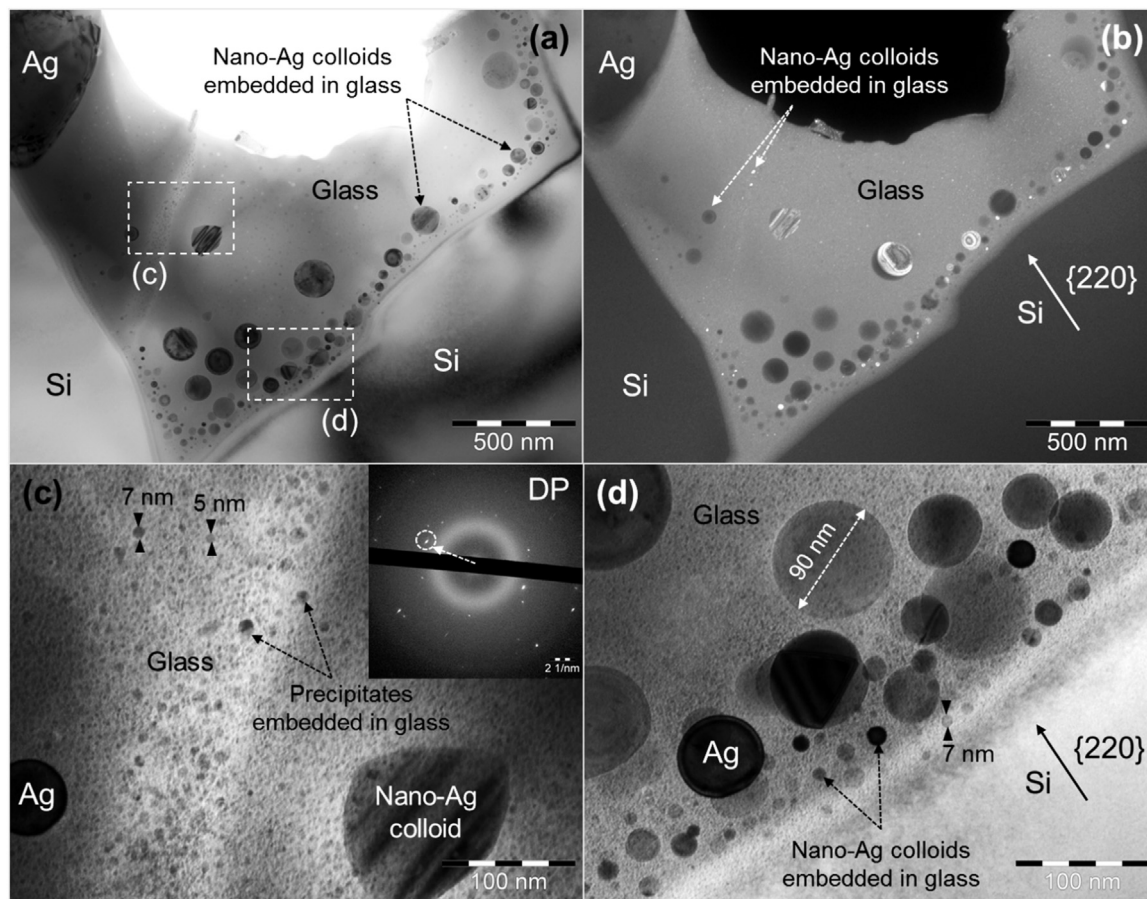


Fig. 3. Low-magnification (a) bright-field, (b) dark-field images of cell #2 (p-type) in plan-view showing the contact interface, (c) and (d) high-magnification bright-field images of the respective rectangular areas marked in (a). Inset in (c) shows an electron diffraction pattern of the glass layer. Nano-Ag colloids of sizes 5–150 nm embedded in the glass layer with larger density compared to cell #1.

interpreted as coming from an amorphous structure (glass) that contains crystalline precipitates. The circular shaped background in the diffraction patterns is due to the amorphous part of the glass layer. Ag (111) and (002) reflections and Si reflections were identified in the glass layer. Additional reflections were identified that belong to other precipitates than the Ag colloids. This is seen best in the corresponding dark-field images. High-magnification dark-field images (see Fig. 4c–d) showed Ag colloids and other precipitates (< 10 nm) dispersed in the glass layer (bright areas in Fig. 4b–d). The presence of precipitates also indicates that in the amorphous phase point defects, i.e. impurities, might be present.

Fig. 5a–b show the low-magnification bright and dark-field images of cell #3 obtained at the Si/metallization interface. The microstructure is very similar to the one observed for cell #2. A local opening of the SiN_x layer and high densities of nano-Ag colloids were observed in the glass layer. Nano-Ag colloids sitting close the Si emitter surface are smaller in size as compared to colloids in the inner part of the glass layer. Diffraction patterns (Fig. 5c) and dark field images were acquired using Ag (111) reflection. This yielded small sized (10 nm) precipitates in the glass layer (see Fig. 5b). These precipitates can be best seen in the thinner part of the glass layer. High-magnification images of the glass layer are shown in Fig. 5d–e. The diameter of nano-Ag colloids was estimated between 5 and 250 nm. The larger nano-Ag colloids are crystalline in nature, as can be seen in Fig. 5d.

3.2. Phase mapping at the Si/metallization interface

In high-efficiency n- and p-type cells the emitter is covered by a 500 nm thick glass layer on top of which the bulk Ag is present. The

microstructure at the Si/metallization interface is complex and therefore, EF-TEM imaging is suitable to effectively examine the essential features of the microstructure by generating phase maps. The combined acquisition of EF-TEM images and EDX spectra turned out to be very useful for the phase mapping.

Fig. 6a–i show the superimposed energy-filtered (EF-) TEM images of cells #1, #2, and #3, acquired at three different energy losses of 16 eV, 24 eV, and 32 eV, respectively. For each cell more than 5–10 different areas were investigated in detail. These images yield optimized contrast for the identification of the phases; Si emitter (pink), the nano-Ag colloids (dark blue) and the glass layer (green). In a next step these phases were quantitative analyzed by TEM-EDX spectroscopy and spectra corresponding to each cell are shown in the [Supporting information S2](#).

The presence of a residual SiN_x layer (Fig. 6a–c) is important for the contact interface analysis. For cell #1, only small pockets of the SiN_x (marked area in Fig. 6a) layer were detected whereas for cells #2 (Fig. 6d–f) and #3 (Fig. 6g–i) a residual SiN_x layer was identified over a large area at the contact interface. In some areas the SiN_x was etched off completely and yielded a reduced density of the nano-Ag colloids in the glass layer. It even appears that the SiN_x layer triggers the density of nano-Ag colloids in the glass layer: with a SiN_x layer locally present, a larger density of nano-Ag colloids was observed. The presence of small precipitates and nano-Ag colloids could be observed in the glass layer. The density of Ag colloids/precipitates is much higher for cells #2 and #3 as compared to cell #1. Additional high-magnification images of the glass layer of cells #1, #2, and #3 are given in the [Supplementary information S3](#).

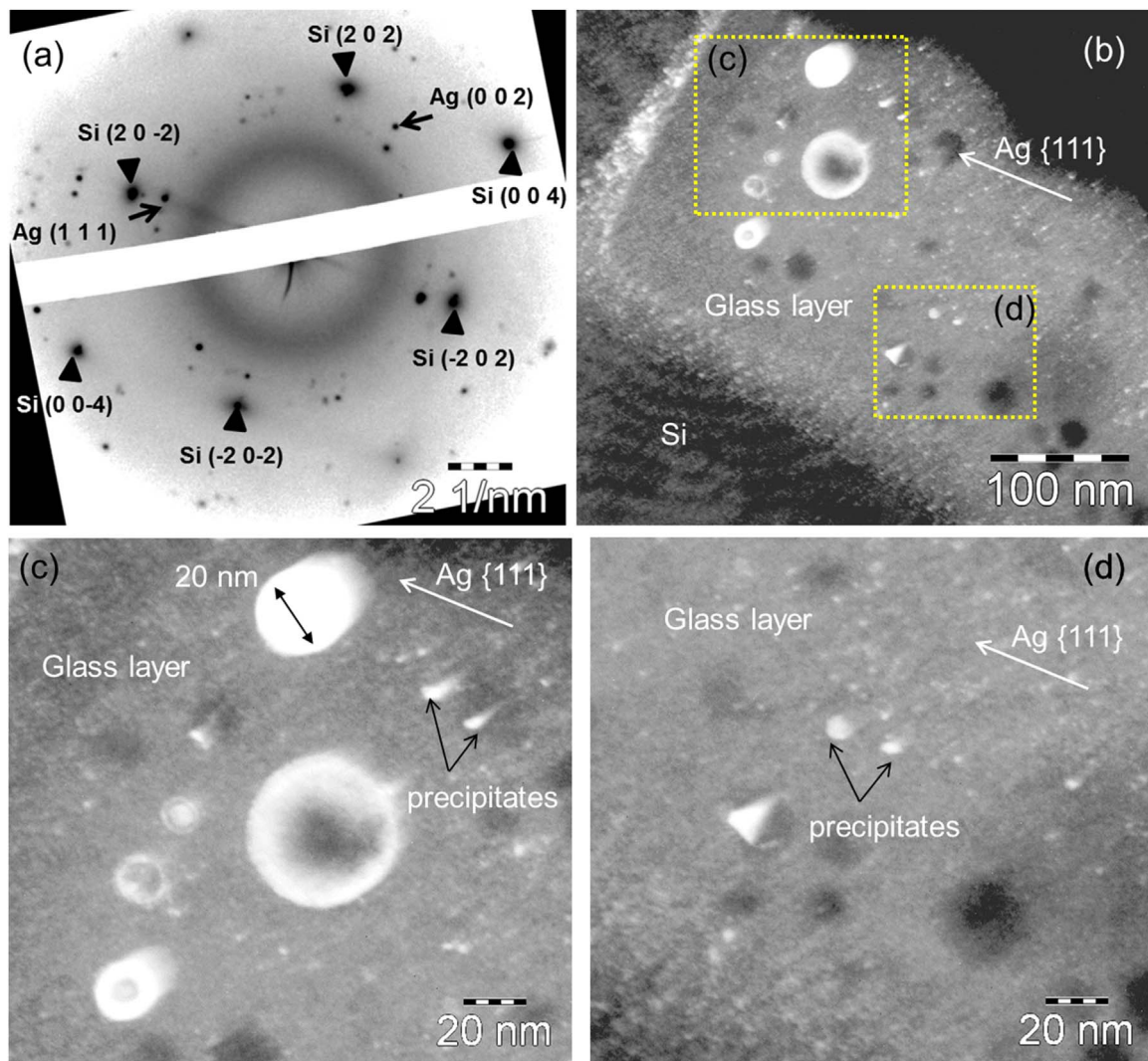


Fig. 4. Diffraction pattern and dark-field images of cell #2 (p-type) obtained at the Si/glass region. Diffraction pattern confirms the presence of Ag reflections in the glass layer. (c–d) show the high-magnification images of the glass layer.

3.3. Quantitative chemical analysis of the glass layer by SEM-EDX spectroscopy

The quantitative chemical analysis of the glass layer of cells #1, #2, and #3 was carried out by SEM-EDX spectroscopy and is summarized in Table 5. SEM-EDX analysis of the glass layer is demanding because the thickness of the glass layer is typically less than 1 μm . Therefore, to reduce the lateral resolution of EDX, 5 keV accelerating voltage was chosen to keep the lateral resolution suitable for the chemical analysis of the glass layer, particularly for the quantification of the light elements O, N and some metallic impurities. Fig. 7a–c show the spectra of cells #1, #2 and #3 plotted in a logarithmic scale to highlight elements with small mole fractions. The chemical composition of the glass layer consists of a Pb containing SiO_x matrix, while additives such as Ag, Zn, Al, Ti were dispersed in the glass layer [6–8]. For cells #2 and #3 Pb mole fractions (5–6 at%) are in the similar range while a slightly higher Pb mole fraction (~ 7 at%) was observed in the glass layer of cell #1. Zn mole fractions of 6.8 at% were detected in the glass layer of cell #1, whereas for cells #2 and #3, Zn mole fractions were in the range of 1–2 at%. An Al mole fraction of ~ 1 at% was detected in the glass layer of cells #2 and #3 but Al was not detected in the glass layer of cell #1.

A boron (B) peak could be detected in the EDX spectrum of the glass phase of cell #1 (Fig. 7a), while P was below the detection limit of the SEM-EDX spectroscopy. Only for cell #2, a P peak could be detected in

the glass layer (Fig. 7b), and the B peak was below the detection limit. Also for cell #3 these elements (P and B) were below the detection limit of EDX.

In summary, for high efficiency p- and n-type cells small mole fractions of Zn (~ 1 at%) and Al (~ 1 at%) were detected in the glass layer. Cells with large Zn (> 5 at%) mole fractions and the absence of Al mole fractions yielded a high contact resistance and a small density of nano-Ag colloids in the glass layer. P and B could be identified only in the glass layer of p-type cells, however, such elements were below the detection limit of the EDX for n-type cells.

3.4. Quantitative chemical analysis of the glass layer by analytical TEM-EDX spectroscopy

Further quantification of the glass layer was investigated by TEM-EDX spectroscopy, especially for the quantification of the additives (Pb, Zn, Al and Ti) and dopant elements (P, B). TEM-EDX is best suited for the quantification of the glass layer. For all cells 10–20 spectra were acquired with a spot size of 32 nm with stray aperture inserted. By this approach the minimum detectable mole fractions could be improved significantly [28].

Table 6 summarizes the chemical composition of the glass layer of cells #1, #2 and #3, respectively. Oxygen was included in the quantification of the glass layer and the spectra corresponding to each cell

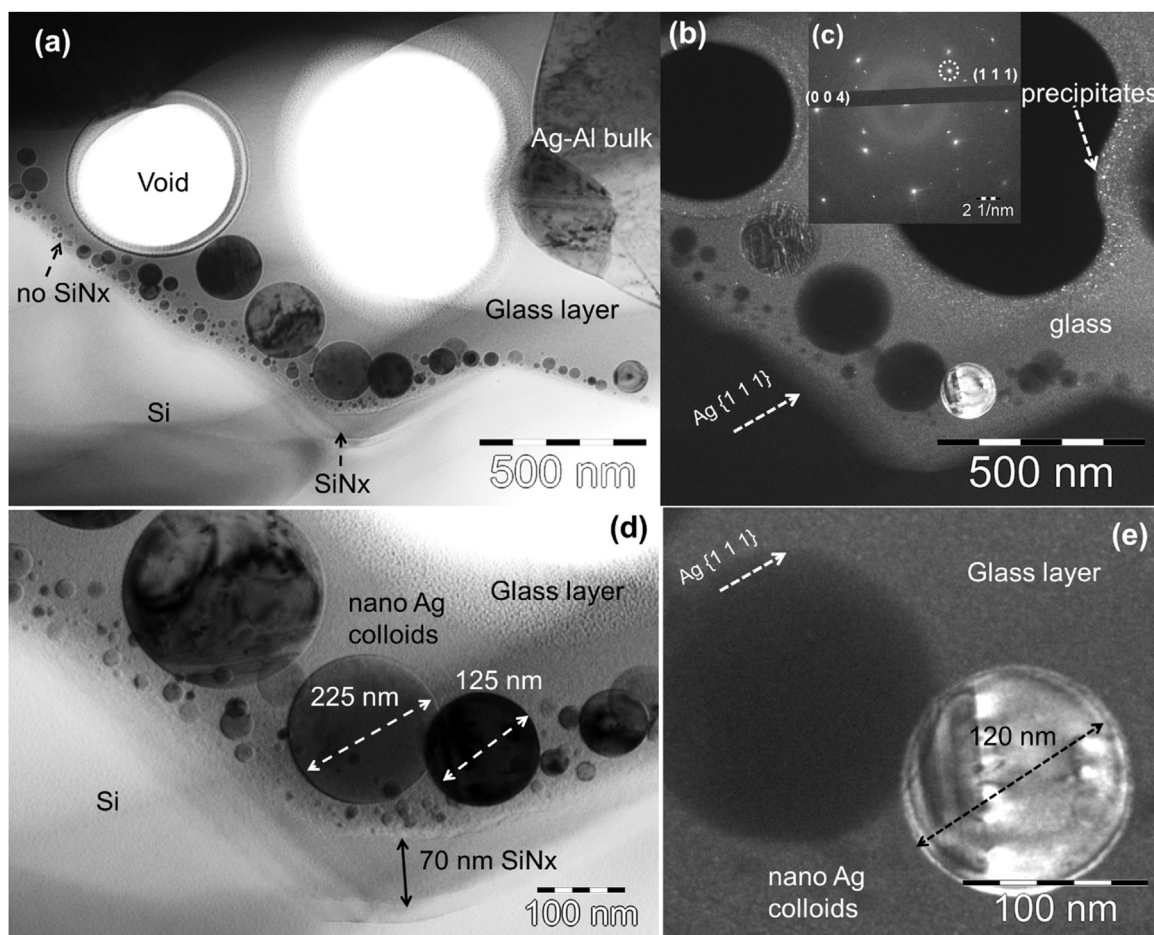


Fig. 5. Low-magnification (a) bright-field and (b) dark-field image of cell #3 (n-type) acquired at the Si/metal contact interface. Inset (c) shows the diffraction pattern at the Si/glass interface area. (d–e) high-magnification bright-field images of the glass layer showing the nano-Ag colloids of sizes 5–225 nm, and (f–g) dark-field image of the glass layer containing crystalline Ag nano-colloids.

are shown in Fig. 8a–c. The glass layer can be understood as a (SiO_x) Pb phase with a Si/Pb mole fraction ratio of ~ 4 for cell #1 and slightly higher ratio of ~ 6 for cells #2 and #3. Consistent with the SEM results, only for cell #1 a significantly higher Zn mole fraction (~ 5 at%) was detected in the glass layer compared to cells #2 and #3 (< 1 at%). The presence of higher Zn mole fractions yielded Zn rich oxide phases (Zn_2SiO_4) embedded in the glass layer as confirmed by EF-TEM images (Fig. 6c).

In a next step, O was excluded from the quantitative analysis of the glass layer to improve the minimum detectable mole fraction of the elements such as B, P and Ti. The results are summarized in Table 7. Details of B and P peaks analysis by SEM and TEM-EDX spectroscopy can be found in the Supplementary information S4.

Fig. 9 shows a correlation diagram of SEM-EDX mole fractions versus TEM-EDX mole fractions of the glass layer plotted in a log-log scale. This diagram correlates the quantitative SEM-EDX data to quantitative TEM-EDX data for a certain microstructure, i.e. glass layer with Ag colloids and precipitates. The mole fractions values are very close in both measurements, i.e. TEM results follow SEM results. This result is not trivial since the acquisition conditions are very different. Since analysis in the SEM-EDX is much less tedious and widely spread than in the TEM, and therefore this result is of great practical value. Only for Ag and Zn mole fractions we observed significant differences: SEM results show higher mole fractions as compared to TEM-EDX. In case of additives/impurity elements such as Ag, Zn, and Al SEM results showed higher mole fraction as compared to the TEM results. This is because of the poor resolution of the SEM. On the other hand TEM yielded more accurate mole fractions of the additives/impurity

elements. The size of the EDX spot in TEM is 30 nm and yields more precise analysis of the glass layer, however, in SEM-EDX spectroscopy if the choice of right parameters such as low primary energy 5 keV was applied we could significantly improve the lateral resolution of SEM-EDX as shown in the correlation diagram. The lateral resolution of SEM-EDX at 20 keV, which is typically applied in the published literature is too poor and, therefore, unfavorable to investigate the glass layer.

Additional correlation diagrams of Pb versus Si and Zn + Pb versus Si mole fractions of cells #1, #2 and #3 can be found in the Supplementary information S5. In the correlation diagram of Fig. S5, it is evident that the glass layer is inhomogeneous with respect to its chemical composition. For both combinations, a negative correlation was observed between Pb and Si and Zn + Pb and Si mole fractions. This indicates that (Pb, Zn) and Si are negatively correlated and, therefore, Pb and Zn both substitute Si.

4. Discussion

Microstructure, structure-property correlation and possible current paths were addressed both for p-type and n-type high-efficiency cells [6,8]. As a major result, it was found that the microstructure of n-type and p-type high-efficiency cells are remarkably similar. The microstructure consists of a glass layer that is less than $1 \mu\text{m}$ thick and embedded Ag colloids which have a volume fraction of up to 20% and bulk Ag fingers are arranged on top of the glass layer. In addition, structure-property correlation of high-efficiency n- and p-type cells yielded similar contact resistance, series resistance and common features of the microstructure of the front side contacts, i.e. a glass layer containing

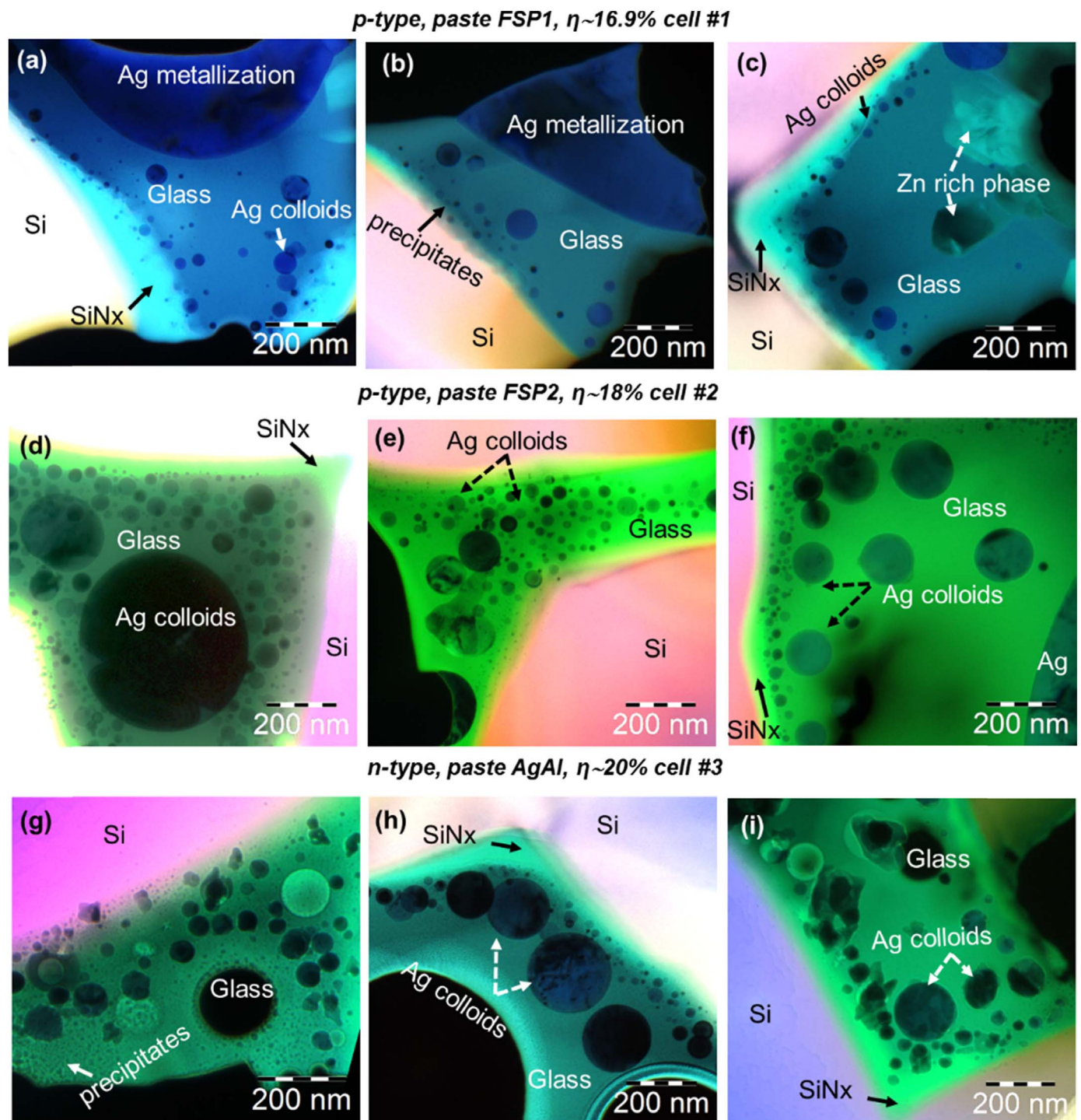


Fig. 6. High-magnification EF-TEM images of the glass layer (a–c) p-type, cell #1, (d–f) p-type, cell #2 and (g–i) n-type, cell #3. Different phases such as Si emitter, glass layer, SiNx layer and Ag colloids/precipitates are identified at the Si/metallization interface.

high density of Ag colloids [6,8]. Only the formation of Ag nanocrystals at the Si emitter is different: in p-type cells Ag nanocrystals are formed, in n-type cells these nanocrystals do not appear [6,8]. Since the series and contact resistance of high efficiency n-type and p-type cells are comparable it is concluded that (pyramidal shaped) Ag nanocrystals at the Si emitter are not necessary for yielding a low contact resistance. Instead a high density of nano-Ag colloids in the glass is more relevant for a low contact resistance [8].

This conclusion contradicts Refs. [3,4,17,18], in which Ag nanocrystals are suggested to be relevant for the low contact resistance and

authors suggested that they contribute significantly to the current path. However, our experimental results do not support this argument but indicated that the glass layer is essential for the current path and that the relevant understanding is a percolation transport model. The Ag colloids constitute current filaments with reduced resistance in the glass layer, thereby introducing a percolative current which is the basis of the proposed model [20]. This model was new and differs from the classical percolation model as it directly relies on the macroscopic resistance of these filaments, and in considering the matrix as semiconducting rather than insulating. The semiconducting matrix is the glass layer and its

Table 5

Quantitative chemical analysis of the glass layer of cells: #1 (p-type), #2 (p-type) and #3 (n-type) carried out by SEM-EDX spectroscopy. Quantitative analysis was done including oxygen and average chemical composition of the glass phase is summarized in the table.

Glass layer	Si [at%]	O [at%]	Ag [at%]	Zn [at%]	Pb [at%]	Al [at%]
Cell #1, paste FSP1	19.4	64.0	3.4	6.8	6.4	–
Cell #2, paste FSP2	28.5	58.6	5.6	1.0	4.9	1.4
Cell #3, paste AgAl	28.8	59.6	4.0	2.4	4.0	1.2

chemical composition and microstructure directly affect its electrical properties.

A second motivation for analyzing the glass layer in detail is due to the screen printing technology. The glass layer is a finger print of the used paste, as will be discussed below. It contains the elements of the paste and generates the precipitation process in which Ag colloids are formed.

We gave two arguments why the analysis of the glass layer is important: (i) understanding the current path and (ii) understanding paste specific differences of the glass layers yielding different series and

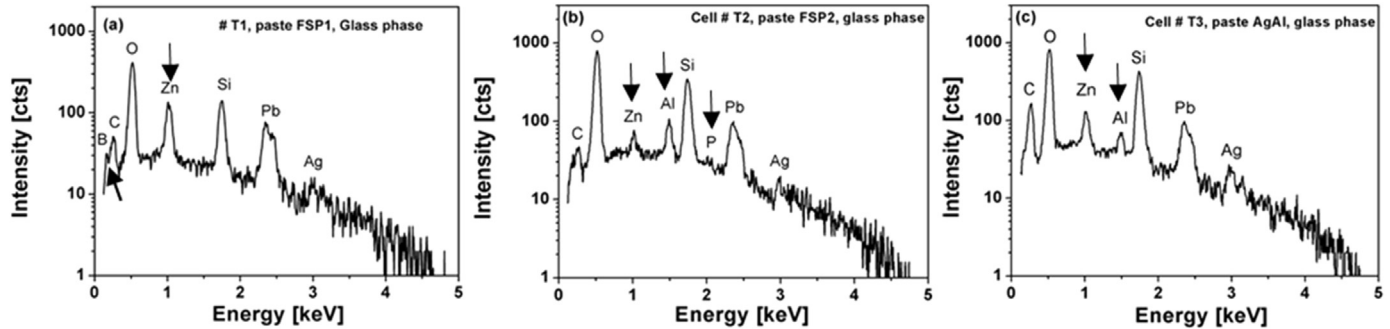


Fig. 7. SEM-EDX spectra of the glass layer obtained on (a) p-type, cell #1, (b) p-type, cell #2, and (c) n-type, cell #3. All spectra were plotted on a logarithmic scale to highlight elements with small mole fractions.

Table 6

Quantitative chemical analysis of the glass layer obtained on cells: #1 (p-type), #2 (p-type) and #3 (n-type) by EDX spectroscopy in TEM. Quantitative analysis was done including oxygen and average chemical composition of the glass phase is listed in the table.

Glass layer	Si [at%]	O [at%]	Ag [at%]	Zn [at%]	Pb [at%]	Ti [at%]	Al [at%]	P [at%]
k-factor	1.00	2.25	1.76	1.54	3.04	1.09	1.03	0.99
Cell #1, paste FSP1	28.71	55.78	2.37	4.58	7.27	1.29	–	–
Cell #2, paste FSP2	34.42	54.78	2.45	0.42	6.47	0.11	1.02	0.33
Cell #3, paste AgAl	36.60	56.20	0.72	0.44	4.60	0.12	1.32	–

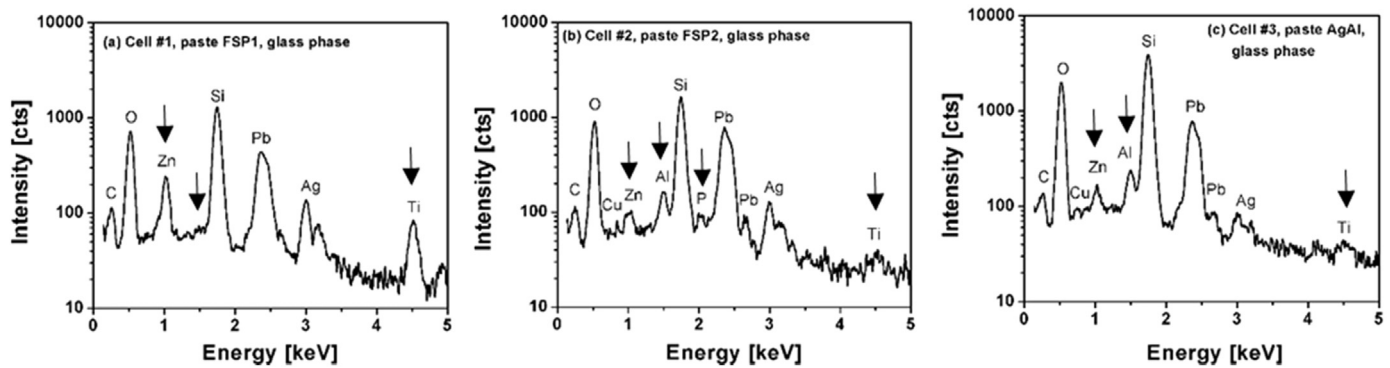


Fig. 8. (a–c) Show the TEM-EDX spectra of the glass layer of cells: (a) p-type, cell #1, (b) p-type, cell #2 and (c) n-type, cell #3, respectively plotted on a logarithmic scale in order to highlight elements with small mole fractions.

Table 7

A detailed quantitative chemical analysis of the glass layer of cells: #1 (p-type), #2 (p-type) and #3 (n-type) was carried out by EDX spectroscopy in TEM. For this O was eliminated from the analysis to improve the quantification of other elements.

Glass layer	Si [at%]	Ag [at%]	Zn [at%]	Pb [at%]	Ti [at%]	Al [at%]	P [at%]
k-factor	1.00	1.76	1.54	3.04	1.09	1.03	0.99
Cell #1, paste FSP1	68.0	4.26	9.69	15.22	2.83	–	–
Cell #2, paste FSP2	74.22	5.38	1.24	15.36	0.22	2.77	0.81
Cell #3, paste AgAl	84.0	1.82	0.97	10.09	0.23	2.89	–

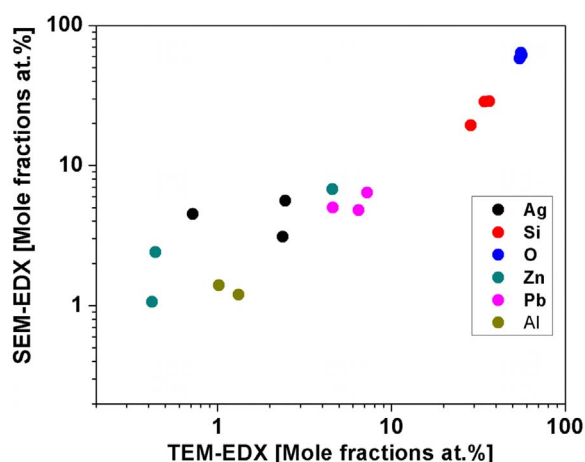


Fig. 9. A log-log plot of correlation diagram of SEM-EDX mole fractions against TEM-EDX mole fractions measured in the glass layer of cell #1 (p-type), and #2 (p-type) and cell #3 (n-type). Quantitative data of six different elements (Ag, Zn, O, Si, Al and Pb) are shown in the plot.

contact resistances. Despite the obvious importance of the glass layer hardly any analysis of its chemical composition has been carried out yet. Our results are the first quantitative analyses directly addressing its chemical composition.

4.1. Microstructure of the glass layer and contact resistance

A key question for understanding the electrical properties of the glass layer is to decide whether it is (i) an insulator or (ii) a semiconductor with significantly reduced resistivity as compared to an insulator. Electrical measurements of the glass layer do not exist, therefore, microstructural analyses will be used to understand its electrical properties. Also temperature dependent measurements of the series resistance are essential for understanding the electrical properties of the glass layer [6,8].

Microstructural features that would transform the insulator, i.e. stoichiometric, amorphous silicon oxide into a dirty semiconducting phase would be: impurities, i.e. point defects, and electrically conducting precipitates. EDX spectroscopy is able to measure the mole fraction of impurities beyond the detection limit, electron microscopy is able to image precipitates and determine their density. This has been done in great detail in this paper. We acquired about 10–20 EDX spectra for each sample in the glass layer. The following elements were found in the glass layer and were significantly above the detection limit of EDX: O, Si, Pb, Ag, Al, Zn and Ti.

The results reported here explicitly address the paste specifications differences both in the microstructure and chemical analysis of the glass layer. High-efficiency cells (#2 and #3) show significantly more nano-Ag colloids and precipitates in the glass layer as compared to cell #1. The density of such precipitates and nano-Ag colloids are paste dependent: (i) for high-efficiency cells #2 (p-type) and #3 (n-type) we observed a high density of precipitates and Ag colloids and a contact resistance of less than $5 \text{ m}\Omega \text{ cm}^2$ and cell efficiencies of 18% for p-type and 20% for n-type, respectively, (ii) for cell #1 a much smaller density of Ag colloids/precipitates in the glass was observed and correlated with a high contact resistance ($20 \text{ m}\Omega \text{ cm}^2$) and hence a low efficiency (16.9%). This indicates that the series and contact resistance of the screen printed front side contacts depend on the microstructural features of the glass layer.

Ionkin et al. reported the influence of nano-Zn grains and micro-Zn pastes on electrical properties such as efficiency, fill factor, and series resistance of the solar cell [31]. The authors concluded that micrometer-sized metallic Zn and ZnO grains are reducing the efficiency of

the crystalline Si solar cells compared to cells contacted with the nano-Zn paste. This is in agreement with our experimental findings for cell #1 wherein we observed a relatively large Zn mole fraction and micrometer sized Zn rich phases in the glass layer. This results in a Zn_2SiO_4 rich oxide phases and an interrupted wetting of the glass layer. In case of high-efficiency cells (#2 and #3) Zn and Al mole fractions in the range of 1–2 at% were detected in the glass layer and therefore yield a more pronounced wetting and a high density of Ag colloids in the glass layer.

These results suggest that the growth of nano-Ag colloids is affected by Zn and Al mole fractions because all other elements were found in the similar range. Given the large number of precipitates found in the glass layers of high-efficiency p- and n-type cells in this study, we assume that current paths across the glass layer, e.g. due to percolation, exist and thus reduce the effective glass layer resistivity. The glass layer is considered to be a dirty semiconductor containing highly conductive Ag colloids and precipitates on a smaller length scale.

4.2. Differences in chemical composition of the glass layer for cells processed with different pastes

The Si/metallization interface consists of a glass layer next to the Si emitter and Ag colloids and precipitates on a smaller length within the glass layer. Paste specific features can be identified by applying imaging and EDX spectroscopy of the glass layer in the TEM. Elemental mapping of such complex interfaces is essential for understanding the paste specific differences and their effect on the electrical properties of the cell.

Zn, Al and Ti mole fractions in the glass layer vary for cells processed with different pastes. The average Pb mole fractions of cells reported here did not change significantly from cell to cell. For cell #1 Zn mole fractions up to 5 at% were detected in the glass layer whereas only ~ 1 at% Zn mole fraction was detected for cells #2 and #3. Al mole fraction of ~ 1 at% was detected in the glass layer of cells #2 and #3, but not detected in the glass layer of cell #1. The paste composition usually is not known, but could be identified by measuring the chemical composition of the glass layer by TEM-EDX.

The effect of wetting the Si emitter surface by the front side metallization paste can be monitored by BSE images in the SEM. Pronounced wetting yields a continuous glass layer (magenta in Fig. 10) at the Si surface (paste FSP2, Fig. 10b), whereas restricted wetting yields a discontinuous glass layer (paste FSP1, Fig. 10a).

P and B could be detected in the glass layer if their concentration exceeded the detection limit of EDX in the TEM. P in the glass might come from the dissolved emitter or impurities added in the form of P_2O_5 [32] in the paste, whereas B could be detected if borosilicate glass was used in the glass frit [8]. Since these elements were not observed in the glass layer of cell #3 and, therefore we consider that they do not play a key role for the reduction of the contact resistance.

4.3. Methodology: accuracies and minimum detectible mole fraction, elements in the glass layer

The chemical composition of the glass layer contains more than 10 elements i.e., Si, Ag, Pb, Al, Ti, Zn, O, P and B and determines the series and contact resistance of the front side metallization contacts. The lateral resolution in the SEM is not sufficient for many of the investigated structures (nano-Ag colloids, precipitates and glass layer etc.) and, therefore, a combination of SEM and TEM-EDX was the method of choice. Among the measurement techniques, TEM is highly relevant for analyzing the microstructure and chemical composition of the glass layer down to sub- μm scale.

The quantitative chemical analysis of the glass layer, especially for the light elements requires improved lateral resolution. Lateral resolution of EDX in the SEM can be substantially improved, if a 5 keV

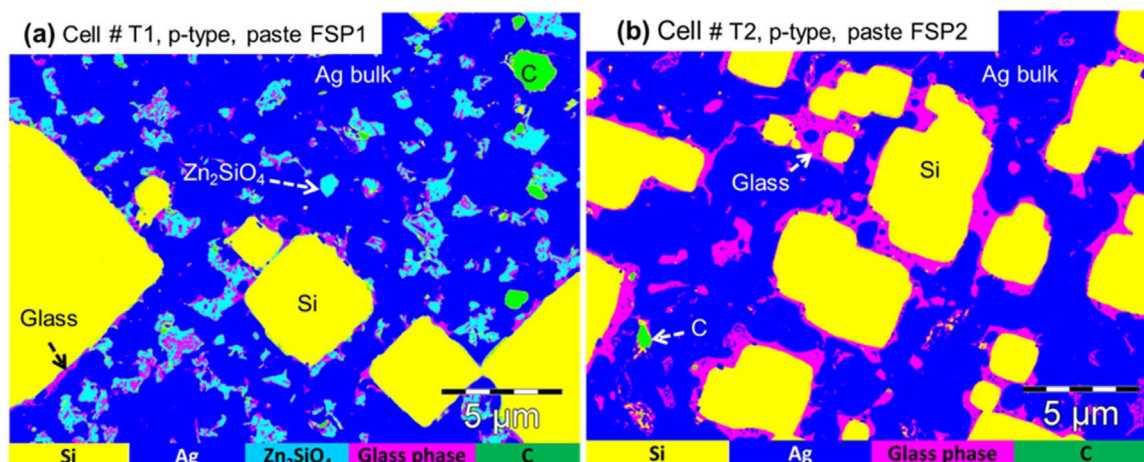


Fig. 10. Plan-view false color backscattered electron (BSE) images are obtained at the Si/Ag interface of (a) a Zn rich paste FSP1, cell #T1 and, (b) a Zn poor paste FSP2, cell # T2. It is evident that Zn rich paste yielded a discontinuous wetting of the glass phase and Zn rich oxide phases at the Si/metalization interface.

primary energy is applied as shown in this work. Spectra acquired under such conditions can be quantitatively analyzed and compared to spectra acquired in the TEM. The Cliff-Lorimer k factor method was used to quantitatively analyze spectra acquired in the TEM [27].

In our recent publication [33], by NanoSIMS (Secondary Ion Mass Spectroscopy) we have shown the effects of the firing conditions on the dopant distributions such as P and B (with a lateral resolution of 80 nm) across the Si/metalization interface and its relation to the series and contact resistance. The quantification as well as imaging of dopants cannot be observed by electron microscopy such as SEM and TEM and, therefore, further analysis of the glass layer by NanoSIMS would be of great interest for imaging precipitates and impurities atoms with a lateral resolution of 100 nm.

5. Conclusions

In this work we report on the microstructure and *quantitative* chemical analyses of the glass layer of high-efficiency n- and p-type Si solar cells by SEM-EDX and TEM-EDX spectroscopy. High-efficiency cells ($\sim 18.0\%$ for p-type and $\sim 20\%$ for n type cells) show similar features: microstructure and chemical composition of the glass layer (a more pronounced wetting and the higher density of nano-Ag colloids), contact resistance less than $5 \text{ m}\Omega \text{ cm}^2$ and the similar temperature dependence of the series resistance.

Given the large density of nano-Ag colloids and other precipitates observed in the glass layer of high-efficiency p- and n-type cells, a *percolative* charge transport across the Si/metalization interface has been proposed.

The chemical composition of the glass layer serves as a chemical bar code of the applied paste used for the screen printing process and affects the contact resistance of the metallization. These findings are of relevance for the paste optimization and charge transport across the Si/metalization interface. The chemical composition of the glass layer is of importance for understanding its microstructural features and its correlation with the electrical properties. The chemical composition of the glass layer was found to be $(\text{SiO}_x)_y \text{Pb}$, elements like Zn, Ti, Al and Ag were detected in the glass layer as impurities. The mole fraction of these elements were above the detection limit of EDX spectroscopy and, therefore, the glass layer is considered as a dirty semiconductor rather than an insulator.

Al and Zn mole fractions (in the range of 1–2 at%) were detected in the glass layer of high-efficiency p- and n-type cells. This implies that the role of additives in the glass layer is essential for the reduction of the contact resistance.

Acknowledgements

We acknowledge the group of D. Biro and F. Clement at the Fraunhofer Institute for Solar Energy Systems in Freiburg for providing high-quality p-type Si solar cells and L.J. Koduvilukalathu and R. Kopecek from ISC-Konstanz for providing high-efficiency n-type Si solar cells.

Appendix A. Supporting information

Supplementary data associated with this article can be found in the online version at <http://dx.doi.org/10.1016/j.solmat.2018.01.001>.

References

- [1] M.M. Hilali, S. Sridharan, C. Khadilkar, A. Shaikh, A. Rohatgi, S. Kim, Effect of glass frit chemistry on the physical and electrical properties of thick-film Ag contacts for silicon solar cells, *J. Electron. Mater.* 35 (2006) 2041–2047.
- [2] M. Hörteis, T. Gutberlet, A. Reller, S.W. Glunz, High-temperature contact formation on n-Type silicon: basic reactions and contact model for Seed-Layer contacts, *Adv. Funct. Mater.* 20 (2010) 476–484.
- [3] G. Schubert, F. Huster, P. Fath, Physical understanding of printed thick-film front contacts of crystalline Si solar cells-review of existing models and recent developments, *Sol. Energy Mater. Sol. Cells* 90 (2006) 3399–3406.
- [4] C. Ballif, D.M. Huljić, G. Willeke, A. Hessler-Wyser, Silver thick-film contacts on highly doped n-type silicon emitters: structural and electronic properties of the interface, *Appl. Phys. Lett.* 82 (2003) 1878–1880.
- [5] D. Pysch, A. Mette, A. Filipovic, S.W. Glunz, Comprehensive analysis of advanced solar cell contacts consisting of printed fine-line seed layers thickened by silver plating, *Prog. Photovolt. Res. Appl.* 17 (2009) 101–114.
- [6] P. Kumar, M. Pfeffer, B. Willsch, O. Eibl, Contact formation of front side metallization in p-type, single crystalline Si solar cells: microstructure, temperature dependent series resistance and percolation model, *Sol. Energy Mater. Sol. Cells* 145 (2016) 358–367.
- [7] P. Kumar, B. Willsch, M. Dürschnabel, Z. Aabdin, R. Hoenig, N. Peranio, et al., Combined microstructural and electrical characterization of metallization layers in industrial solar cells, *Energy Procedia* 67 (2015) 31–42.
- [8] P. Kumar, M. Pfeffer, B. Willsch, O. Eibl, V.D. Mihailitchi, L.J. Koduvilukalathu, R. Kopecek, N-type single-crystalline Si solar cells: front side metallization for solar cells reaching 20% efficiency, *Sol. Energy Mater. Sol. Cells* 157 (2016) 200–208.
- [9] R. Hoenig, M. Duerschnabel, W. Van Mierlo, Z. Aabdin, J. Bernhard, J. Biskupek, et al., The nature of screen printed front side silver contacts – results of the project mikrosol, *Energy Procedia* 43 (2013) 27–36.
- [10] Z.G. Li, L. Liang, L.K. Cheng, Electron microscopy study of front-side Ag contact in crystalline Si solar cells, *J. Appl. Phys.* 105 (2009) 066102.
- [11] L. Liang, Z.G. Li, L.K. Cheng, N. Takeda, A. Carroll, Microstructure characterization and current conduction mechanisms of front-side contact of n-type crystalline Si solar cells with Ag/Al pastes, *J. Appl. Phys.* 117 (2015) 215102–215107.
- [12] R. Kopecek, T. Buck, J. Libal, R. Petres, K. Wambach, R. Kinderman, et al., Large area N-type multicrystalline silicon solar cells with b- emitter: efficiencies exceeding 14%, in: *Proceedings of the International Photovoltaic Science and Engineering Conference*, 2005, pp. 3–4.
- [13] R. Lago, L. Pérez, H. Kerp, I. Freire, I. Hoces, N. Azkona, et al., Screen printing metallization of B emitters, *Prog. Photovolt. Res. Appl.* 18 (2010) 20–27.
- [14] S. Fritz, K. Markus, S. Riegel, A. Herguth, H. Matthias, Formation of Ag/Al screen-

- printing contacts on B emitters, *IEEE J. Photovolt.* 5 (2015) 145–151.
- [15] S. Fritz, J. Engelhardt, S. Ebert, G. Hahn, Contacting boron emitters on n-type silicon solar cells with aluminium-free silver screen-printing pastes, *Phys. Status Solidi RRL* 10 (2016) (2016) 305–309.
- [16] H.-S. Kim, S.-B. Cho, H. Kim, D. Kim, M. Dovrat, G. Eytan, J.-Y. Huh, Electrochemical nature of contact firing reactions for screen-printed silicon solar cells: origin of “gray finger” phenomenon, *Prog. Photo.: Res. Appl.* 24 (2016) 1237–1250, <http://dx.doi.org/10.1002/pip.2783>.
- [17] S. Kontermann, G. Willeke, J. Bauer, Electronic properties of nanoscale silver crystals at the interface of silver thick film contacts on n-type silicon, *Appl. Phys. Lett.* 97 (2010) 10–13.
- [18] E. Cabrera, S. Olibet, J. Glatz-Reichenbach, R. Kopecek, D. Reinke, G. Schubert, Experimental evidence of direct contact formation for the current transport in silver thick film metallized silicon emitters, *J. Appl. Phys.* 110 (2011) 114511–114515.
- [19] R.T. Tung, Schottky barrier height—do we really understand what we measure? *J. Vac. Sci. Technol. B Microelectron. Nanometer Struct.* 11 (1993) 1546, <http://dx.doi.org/10.1116/1.586967>.
- [20] M. Pfeffer, P. Kumar, O. Eibl, High efficiency, crystalline Si solar cells with screen printed front side metallization: a percolation model for explaining the current path, *J. Electron. Mater.* 45 (2016) 5764–5772.
- [21] S. Bin Cho, H.S. Kim, J.Y. Huh, Mechanism underlying the beneficial effect of forming gas annealing on screen-printed Ag contacts of crystalline Si solar cells, *Acta Mater.* 70 (2014) 1–7.
- [22] K.K. Hong, S. Bin Cho, J.S. You, J.W. Jeong, S.M. Bea, J.Y. Huh, Mechanism for the formation of Ag crystallites in the Ag thick-film contacts of crystalline Si solar cells, *Sol. Energy Mater. Sol. Cells* 93 (2009) 898–904.
- [23] M.M. Hilali, M.M. Al-Jassim, B. To, H. Moutinho, A. Rohatgi, S. Asher, Understanding the formation and temperature dependence of thick-film Ag contacts on high-sheet-resistance Si emitters for solar cells, *J. Electrochem. Soc.* 152 (2005) G742.
- [24] T.K. Nakajima, A. A. Tada, Ohmic contact of conductive silver paste to silicon solar cells, *Int. J. Hybrid. Microelectron.* 6 (1983) 580–586.
- [25] P.D.C. King, T.D. Veal, Conductivity in transparent oxide semiconductors, *J. Phys.: Condens. Matter* 23 (2011) 334214.
- [26] Y.P. Zhang, Y.X. Yang, J.H. Zheng, G.R. Chen, C. Cheng, J.C.M. Hwang, B.S. Ooi, A. Kovalskiy, H. Jain, Effect of the interface glass on electrical performance of screen printed Ag thick-film contacts of Si solar cells, *Thin Solid Films* 518 (2010) E111–E113.
- [27] V.D. Mihailitchi, J. Jourdan, A. Edler, R. Kopecek, R. Harney, D. Stichtenoth, J. Lossen, T.S. Böschke, H.-J. Krokoszinski, Screen printed n-type silicon solar cells for industrial application, in: *Proceedings of the 25th European Photovoltaic Solar Energy Conference and Exhibition*, 2010, pp. 6–10. doi:<http://doi.org/10.4229/25thEUPVSEC2010-2DO.2.2>.
- [28] N. Peranio, O. Eibl, Quantitative EDX microanalysis of Bi₂Te₃ in the TEM, *Phys. Status Solidi A* 204 (2007) 3243–3255.
- [29] P. Kumar, M. Pfeffer, N. Peranio, O. Eibl, S. Bäßler, H. Reith, K. Nielsch, Ternary, single-crystalline Bi₂(Te, Se)₃ nanowires grown by electrodeposition, *Acta Mater.* 125 (2017) 238–245.
- [30] P. Kumar, M. Pfeffer, E. Schweda, O. Eibl, J. Qiu, Z. Shi, PbSe mid-IR photoconductive thin films (Part I): phase analysis of the functional layer, *J. Alloy. Compd.* 724 (2017) 316–326.
- [31] A.S. Ionkin, B.M. Fish, Z.R. Li, M. Lewittes, P.D. Soper, J.G. Pepin, A.F. Carroll, Screen-printable silver pastes with metallic nano-zinc and nano-zinc alloys for crystalline silicon photovoltaic cells, *ACS Appl. Mater. Interfaces* 3 (2011) 606–611.
- [32] A.F. Carroll, K.W. Hang, B.J. Laughlin, K.R. Mikeska, Conductive compositions and processes for use in the manufacture of semiconductor devices: flux materials inventors, E.I. Dupont De Nemours and Company, United States patent US 8,187,505, 2012, May 29.
- [33] P. Kumar, M. Pfeffer, B. Willsch, O. Eibl, L. Yedra, S. Eswara, J.-N. Audinot, T. Wirtz, Direct imaging of dopant distributions across the Si-metallization interfaces in solar cells: correlative nano-analytics by electron microscopy and NanoSIMS, *Sol. Energy Mater. Sol. Cells* 160 (2017) 398–409.